# Spin-inversion mechanisms in $O_2$ binding to a model heme complex revisited by density function theory calculations

Kohei Saito, Yuya Watabe, Takashi Fujihara, Toshiyuki Takayanagi*

Department of Chemistry, Saitama University, Shimo-Okubo 255, Sakura-ku, Saitama City, Saitama 338-8570, Japan

Jun-ya Hasegawa

Institute of Catalysis, Hokkaido University, Kita 21, Nishi 10, Kita-ku, Sapporo, Hokkaido 001-0021, Japan

**Abstract**

Spin-inversion mechanisms in $O_2$ binding to a model heme complex, consisting of Fe(II)-porphyrin and imidazole, were investigated using density-functional theory calculations. First, we applied the recently proposed mixed-spin Hamiltonian method to locate spin-inversion structures between different total spin multiplicities. Nine spin-inversion structures were successfully optimized for the singlet-triplet, singlet-quintet, triplet-quintet and quintet-septet spin-inversion processes. We found that the singlet-triplet spin-inversion points are located around the potential energy surface region at short Fe-O distances, whereas the singlet-quintet and quintet-septet spin-inversion points are located at longer Fe-O distances. This suggests that both narrow and broad crossing models play roles in $O_2$ binding to the Fe-porphyrin complex. To further understand spin-inversion mechanisms, we performed on-the-fly Born-Oppenheimer molecular dynamics calculations. The reaction coordinates, which are correlated to the spin-inversion dynamics between different spin multiplicities, are also discussed.

---

*Corresponding author, *e-mail*: tako@mail.saitama-u.ac.jp

## 1. Introduction

Understanding the mechanism of spin state changes in $O_2$ binding to heme protein, which contains Fe(II)-porphyrin complexes, has long been an important subject in biochemistry.[1–3] Previous studies have shown that the ground spin state of heme is the high-spin quintet state, whereas that of heme with $O_2$ attached is the low-spin singlet state. Because ground state $O_2$ is in the triplet spin state, $O_2$ binding to heme must involve multiple spin-inversion processes. Spin inversion is alternatively called spin-forbidden, spin-crossover, or intersystem crossing. Theoretically, the spin-inversion process is induced by sizable relativistic spin-orbit couplings of heavy elements, such as transition metal atoms. Thus, the spin quantum number defined in a nonrelativistic electronic Hamiltonian framework is no longer a good quantum number due to strong spin mixing induced by relativistic spin-orbit effects.

Many theoretical studies have investigated atomic-level spin-inversion mechanisms in $O_2$ binding with a simplified model heme, namely, a Fe(II)-porphyrin complex with a proximal imidazole or a related ligand.[4–26] These theoretical studies have shown that the electronic ground state of the Fe(II)-porphyrin complex with a $d^6$ configuration is a quintet spin state and that the second lowest spin state is a triplet state, although the energy difference between these spin states is very small.[3] This spin state property means that $O_2$ binding to the Fe(II)-porphyrin complex can occur on the four potential energy surfaces with singlet, triplet, quintet, and septet spin states. Therefore, previous theoretical studies have mainly focused on identifying the crossing points of these four potential energy surfaces. Two different spin-inversion mechanisms have been proposed so far: broad and narrow crossing region models.[1, 13] In the broad crossing region model, spin inversion mainly occurs at longer Fe–$O_2$ distances, for which the corresponding potential energy surfaces with different spin states of the $O_2$-heme system are nearly degenerate. This mechanism was derived from reduced-dimensionality calculations of the potential energy surfaces using preselected molecular coordinates, such as Fe–O distance and deformation distance of Fe from the porphyrin plane.[4, 5, 13] Therefore, the crossing points in the reduced-dimensionality potential energy surfaces do

not correspond exactly to the crossing points in full dimensions. The narrow crossing region model suggests that specific singlet-triplet crossing points, which should occur at shorter Fe–$O_2$ distances, play an essential role in the overall spin-inversion processes. Hasegawa and coworkers recently succeeded in optimizing the crossing point structure between the singlet and triplet potential energy surfaces in full dimensions.[15] However, systematic crossing point searches for other spin states have not yet been performed.

Against this background, here we report more systematic computational results to elucidate the spin-inversion mechanisms in $O_2$ binding to the model Fe(II)-porphyrin-imidazole complex using two different approaches. The first is the mixed-spin Hamiltonian method, where two potential energy surfaces with different spin states are artificially coupled through spin-orbit coupling.[27–31] This method enables the efficient optimization of a spin-inversion structure of the two different potential energy surfaces as a transition state on the mixed-spin potential energy surface. Thus, the spin-inversion process can be easily understood by calculating the intrinsic reaction coordinate (IRC) path, similar to the electronically adiabatic case. The second approach is the Born-Oppenheimer molecular dynamics (BOMD) method, where the $O_2$ capture by the Fe(II)-porphyrin-imidazole complex is traced directly using on-the-fly classical trajectory calculations on the potential energy surface with the specific spin state. The crossing points are subsequently analyzed along the calculated trajectories. These two computational approaches are expected to provide a clear picture of the spin-inversion mechanisms of $O_2$ binding to the model Fe(II)-porphyrin-imidazole complex.

## 2. Computational details

Our computational model consisted of a Fe(II)-porphyrin complex ($FeC_{20}N_4H_{12}$) with a proximal imidazole ($C_3N_2H_4$), which is called FePorIm hereinafter. This model compound is the most extensively used in theoretical studies.[4–9,11–16,20] Throughout this study, we employed density functional theory (DFT) calculations with the B97D exchange-correlation functional because the B97D functional including empirical

dispersion corrections showed good performance in calculations of 3d transition metal compounds.[32] This functional also performed well for calculating the relative energy of spin states in Fe complexes[33] and the $O_2$ binding energy in the $O_2$-FePorIm complex.[9] It should be emphasized that the importance of dispersion correction in $O_2$ binding to heme has been also found in Refs. 9 and 14. We used the standard 6-311+G* basis sets for Fe and O atoms, and the 6-31G** basis sets for C, N, and H atoms. These somewhat small basis sets have been chosen to reduce computational time of the BOMD calculations. The accuracy of the present approach will be described in the next section. The spin-unrestricted DFT calculations were performed using the Gaussian09 program package.[34]

As mentioned in Introduction, $O_2$ binding to the Fe(II)-porphyrin complex can occur on the potential energy surfaces with four spin states, i.e., singlet, triplet, quintet, and septet. We considered only the lowest-lying electronic state for each spin multiplicity at a given geometry. This has been achieved by using the "stable = opt" option implemented in the Gaussian09 program package[34] , which generally leads to the lowest-energy SCF solution. As for the highest septet spin state, the spin density distributions on Fe and $O_2$ show the same majority spin (i. e., $\alpha$-spin), with the spins of $O_2$ and Fe being approximately triplet and quintet, respectively. For the intermediate quintet state, the spin-flipping mainly occurs on the Fe site from the above septet spin state. In the case of the singlet spin state, the spin on the $O_2$ moiety further flips, where the corresponding spin density indicates an antiferromagnetic coupling between the $O_2$ and FePorIm moieties. Thus, this singlet state is corresponding to the open-shell singlet configuration which can be obtained from the spin-unrestricted broken-symmetry calculations. The spin densities are presented Figures S1-S3 in Supporting Information.

For each singlet, quintet, or septet spin state, our geometry optimization for the $O_2$-FePorIm complex yielded four optimized structures (due to the 4-fold occupancy of $O_2$ addition to porphyrin) with the same spin configuration. In the case of the triplet spin state, however, geometry optimization yielded two types of structures with different spin configurations. These two spin states were called $T_1$ and $T_2$ in Ref. 15. In the former $T_1$ configuration, $O_2$ has an original triplet character even in the $O_2$-FePorIm complex and thus the $O_2$ moiety and the FePorIm moiety have opposite spin characters (i. e., $\alpha$- and $\beta$-

spin, respectively). This can be easily confirmed from the spin density plot. On the contrary, in the $T_2$ configuration, the same spin is distributed over both the $O_2$ and FePorIm moieties. Due to these different spin distribution characters, the triplet potential energy surface yields two types of equilibrium structures; the equilibrium structures with the $T_1$ triplet configuration occur at *R*(Fe-O) ~ 2.18 Å while those with the $T_2$ configuration occur at shorter *R*(Fe-O) ~ 1.86 Å due to a small $O_2^-$ contribution via electron transfer from Fe(II). In addition, it was found that the imidazole orientation is also different between these two configurations. Since the $T_2$ minima are energetically more stable than the $T_1$ minima, BOMD calculations starting from long *R*(Fe-O) distances do not sample the $T_1$ minima on the triplet potential energy surface, as shown later. Detailed information on the geometric structures with the $T_1$ and $T_2$ spin configurations as well as their spin densities is presented in Supporting Information.

We used the mixed-spin (2 × 2) Hamiltonian matrix approach to optimize the spin-inversion structures,[27–31] where two potential energy surfaces with high-spin and low-spin multiplicities were mixed through the preassumed spin-orbit coupling parameter of 100 $cm^{-1}$. This spin-orbit coupling value was used to optimize spin-inversion structures efficiently. The coupling parameter used in this work was sufficiently small and did not significantly affect the original potential energy surface shape at the molecular structure deviating from the spin-inversion point.[28–31] First, we used the upper eigenstate of the (2 × 2) Hamiltonian matrix, and then we performed standard geometry optimization to find a potential energy minimum on the upper mixed-spin potential energy surface. The optimized structure on this upper surface was a good initial structure for transition state optimization on the lower mixed-spin potential energy surface, which corresponded to the spin-inversion structure between the two potential energy surfaces with different spin states. After optimizing the transition state structure, we performed the standard IRC calculations to identify the reaction pathway. We used Gaussian09 code and Global Reaction Route Mapping code[35–39] in this computational scheme. For the optimized spin-inversion structures, we also calculated spin–orbit coupling using MolSOC software, [40] where the spin–orbit coupling matrix elements were generated from the Breit–Pauli Hamiltonian using the calculated B97D orbitals.

To further understand the spin-inversion processes in more detail, we performed on-the-fly direct trajectory calculations on the B97D-level potential energy surface with a specific spin state. We used the BOMD method implemented in the Gaussian09 package.[34] The BOMD method uses a fifth-order polynomial fitted to the energy, gradient, and Hessian at each time step, and then the step size is taken to be much larger than the step size used in the normal method, employing only the gradient information.[41] At each structure on the calculated trajectory, we performed single-point B97D calculations for other spin states.

## 3. Results and discussion

We optimized the equilibrium structures of the $O_2$-FePorIm complex in each spin state (from singlet to septet) at the B97D level of theory. $O_2$ adopts a 4-fold occupancy for each spin state due to the $D_{4h}$ symmetric property of the isolated porphyrin molecule.[5] Figure 1 shows one of the four binding structures and the other structures (including the optimized structures with the $T_1$ spin configuration) are presented in Figures S1, S2 and S3 of Supporting Information. The four structures in each spin state have comparable energies (energy differences smaller than 1 kcal/mol). For the singlet and triplet states, the imidazole ligand has a staggered conformation with a $C_{im}–N_{im}–Fe–N_{por}$ torsional angle of ~45° in the optimized structures. In contrast, for the quintet and septet states, the imidazole ligand has a different configuration with a $C_{im}–N_{im}–Fe–N_{por}$ torsional angle of ~0°. The optimized structures for the singlet and triplet states are similar, with Fe–O bond lengths of 1.85 and 1.86 Å, respectively, indicating that there is a strong Fe–O bond in these two spin states. However, the optimized Fe–O–O angles for the singlet and triplet states are somewhat different (121.1° and 132.7°, respectively). It is also interesting to note that the optimized structures for the quintet and septet state are similar with long Fe–O distances of 2.92 and 2.88 Å, respectively. These overall similarities in the optimized geometries suggest that there is a spin-inversion transition state between the two equilibrium structures with singlet–triplet and quintet–septet spin multiplicities. We

have also performed NBO calculations to further understand Fe-O and O-O bonding nature. The result of the NBO calculations is presented in Table S1 of Supporting Information and the Fe–O distances in the optimized structures are found to be consistent with the calculated bond-order values.

Before presenting the spin-inversion structures, we show one-dimensional potential energy curves for the four spin states as a function of the Fe–O distance; this type of potential energy curve has been used in many previous studies.[4,5,12,13,15,16,20] The potential energy curves obtained from the B97D calculations are shown in Figure 2, where other geometrical parameters were fully optimized at each fixed Fe–O distance. The singlet and triplet potential energy curves are similar and the energies around the potential minima are also close. In addition, the quintet and septet potential energy curves are also similar and have shallow potential wells around $R$(Fe-O) ~ 2.9 Å. The figure clearly shows five crossing points among these four potential energy curves; however, it should be emphasized that these crossing points do not correspond to true crossing points in full dimensions, as mentioned in the Introduction. A more careful treatment is required to understand the crossing behavior because the present model system has many nuclear degrees of freedom. At this point, it may be important to provide some comments on the accuracy of the present B97D calculations. As shown in Figure 2, the $O_2$ binding energy is calculated to be 16.6 kcal/mol. This value is larger than the previous value (11.7 kcal/mol) obtained from the same B97D functional but with somewhat larger basis sets.[14] This indicates the importance of the flexible basis sets to obtain an accurate $O_2$ binding energy. It is worth mentioning that the $O_2$ binding energy is also calculated with the highly-correlated CASPT2 method to be 14.9 and 9.9 kcal/mol in Refs. 7 and 9, respectively. Another important point seen in Figure 2 is that the energy gap between the singlet and triplet minima is smaller than the previously reported values.[4–7,9,13–15] This behavior is also due to the small basis sets used as well as the chosen B97D functional. More systematic calculations including scalar relativistic correction should be performed to obtain more accurate potential energy surfaces.

To understand the crossing behavior in full dimensions, we performed a transition state search on the mixed-spin potential energy surfaces using the

computational scheme described in Section 2. As a result, we successfully found nine spin-inversion transition state structures (Figure 3). The corresponding IRC profiles are shown in Figure 4. The barrier heights for these spin-inversion processes are relatively low. For example, the barrier heights measured from the triplet minimum to the singlet minimum are less than 0.5 kcal/mol. The barrier heights measured from the septet minimum to the quintet minimum are calculated to be only 0.4 kcal/mol. Similarly, the barriers from the quintet to the singlet state are calculated as less than 0.1 kcal/mol. These results suggest that the singlet-triplet, quintet-septet, triplet-quintet and quintet-singlet spin inversions may energetically occur in $O_2$ binding dynamics to the model heme complex. In Figure 4, we also show the important geometric parameters for these spin-inversion processes. In the singlet-triplet spin-inversion pathway, the contribution of the Fe–O–O angle is important, suggesting that excitation of the Fe–O–O bending motion may increase the spin-inversion efficiency. In contrast, distance *d*, which is defined as the deviation of Fe from the porphyrin location (Fe out-of-plane distance), plays an important role in the quintet-septet and quintet-singlet spin-inversion processes.

Figure 3 shows the spin-orbit coupling constants (maximum and averaged values) calculated at the optimized spin-inversion structures. The averaged spin-orbit coupling constant is defined as

$$\mathrm{ave}(H^{SO}) = \sqrt{\sum_{i,j} |H_{i,j}^{SO}|^2/(2S_1+1)(2S_2+1)}, \qquad (1)$$

where $H_{i,j}^{SO}$ represents each matrix element and $S_1$ and $S_2$ are the spin multiplicities for the low- and high-spin states, respectively. We report only the maximum value and average value of the spin-orbit coupling elements because for the quintet/septet spin change, the corresponding matrix consists of 35 (= 7 × 5) coupling elements (full complete matrix elements are provided in Supporting Information). We did not calculate the spin-orbit couplings for the singlet-quintet spin inversion because the corresponding couplings are expected to be small. In this case, the direct spin-orbit coupling between the two electronic states is zero and a non-zero coupling can be introduced only from

second-order and higher-order corrections, which are mediated by other electronic states.[42–44] The spin-orbit coupling values are relatively large and are comparable to thermal energy. Although we succeeded in finding these spin-inversion structures from the present transition state search calculations, we could not locate other crossing points (singlet-septet and triplet-septet) at this stage.

Next, we present the results of BOMD calculations. Figure 5 shows the results of the BOMD calculations on the triplet potential energy surface, where the initial distance between O and Fe is set to 3.3 Å with other coordinates optimized on the triplet surface (Figure 2). We also added a small transitional energy (1 kcal/mol) for the approach of $O_2$ and Fe(II)PorIm and the trajectory was calculated up to $t \sim 1$ ps. Figure 5(a) presents the potential energy profiles for the four spin states plotted as a function of time along the BOMD trajectory propagated on the triplet surface. Figures 5(b)–(d) show the change in selected geometric parameters as a function of time. There are six crossing points between the singlet and triplet states along this trajectory. The structures of these crossing points are close to the singlet-triplet spin-inversion structures presented in Figure 3. The important coordinate for the singlet-triplet spin-inversion process is the Fe-O-O bending angle. It is seen that the Fe-O-O bending motion is highly excited for this trajectory, leading to the passage over the crossing point. Also, the Fe out-of-plane distance, *d*, is initially negative, meaning that Fe(II) is located at the other side of the porphyrin plane, although it oscillates around zero once the Fe-O bond is formed ($t > 250$ fs). The potential energy profile shown in Figure 5(a) shows three crossing points between the quintet and septet states.

We performed a similar BOMD calculation for the quintet spin state. The calculation started at $R$(Fe-O) = 3.4 Å and the results are presented in Figure 6. In this case, the initial approach of Fe and O is followed by almost constant distance of $R$(Fe-O) ~ 3 Å up to $t \sim 1$ ps. This is unsurprising because the structure fluctuates around the shallow potential well on the quintet surface (Figure 2). The potential energy profiles of the four spin states are presented in Figure 6(a) and are relatively flat. However, it is interesting to note that two crossing points can be seen between the singlet and quintet surfaces at $t \sim 470$ fs and $t = 610$ fs. In addition, the potential energy surfaces for these

two states are always close in energy. Figures 6(c) and 6(d) show that these crossing points weakly correlate with the motions along the Fe out-of-plane coordinate, *d*, and the Fe-O-O angular coordinate.

The BOMD results for the trajectory in the septet state are shown in Figure 7. There are no clear crossing behaviors between different spin states, although the singlet and quintet potential energy values are nearly degenerate at $t > 600$ fs. Similar to the quintet case, the Fe(II)PorIm complex always stays at the shallow potential well around $R$(Fe-O) ~ 3 Å on this trajectory. However, there is an important difference in the BOMD results between the quintet and septet spin states. In the case of the quintet spin state, the Fe out-of-plane coordinate, *d*, is $-0.17 \le d \le -0.07$ Å, whereas for the septet spin state, *d* is $-0.29 \le d \le -0.19$ Å. This can be readily understood from the optimized structures for the quintet and septet states shown in Figure 1. Therefore, these two trajectories are sampling completely different structural spaces.

To further understand the correlation between the motion along the *d*-coordinate and spin-inversion process, we artificially added an initial kinetic energy to the Fe atom along this coordinate. Again, it should be emphasized that the importance of the Fe out-of-plane distance in $O_2$ binding has been frequently highlighted in previous static DFT calculations.[4,5,6,15,16,20] A recent nonadiabatic quantum wave packet simulation study on photolysis of the CO-bound heme also showed that the Fe out-of-plane motion plays an essential role in the spin-crossover dynamics.[45]

The results of the BOMD calculations in which we added 10 kcal/mol kinetic energy to the Fe out-of-plane motion on both the quintet and septet spin states are shown in Figure 8. Figures 8(c) and 8(g) show larges fluctuations in *d* as a function of time compared with the results in Figures 5(c)–7(c). Figure 8(a) shows several crossings between different spin states for the BOMD trajectory on the quintet spin state. In particular, there are five triplet-septet crossings that are not in Figure 5. Similarly, for the trajectory in the septet state, the singlet and quintet potential energies are always close. These results indicate that the out-of-plane motion of Fe plays a role in spin state crossing in $O_2$ binding to heme.

It is currently unclear whether a surface hopping picture always works well in

spin-inversion reaction systems with many degrees of freedom[46] although simple calculations using the Landau-Zener method have been extensively employed in previous theoretical studies (see also Refs. 47 and 48). Very recent studies using a more sophisticated quantum dynamics on a simple $GeH_2$ system, however, have concluded that such simple Landau-Zener-like calculations significantly underestimate the efficiency of nonadiabatic spin-inversion.[49, 50] This is probably due to the importance of nonlocal nonadiabatic transitions missing in one-dimensional description. Thus, nonadiabatic quantum dynamics calculations, which can take into account the spin-vibronic effects,[46] should be performed to fully understand the spin-inversion mechanisms in $O_2$ binding to the heme complex. In fact, the energy differences between different spin multiplicities in the long Fe-O distance region can be small and are comparable to the magnitude of spin-orbit couplings. In such a case, the spin state dynamics and the associated nuclear dynamics cannot be described independently due to the strong mixing of different spin states. Because it would be impossible to carry out full-dimensional quantum dynamics calculations for the $O_2$-FePorIm system, we are currently planning to perform reduced-dimensionality nonadiabatic quantum wave packet calculations. In addition, it is also important to understand the spin-vibronic effects of the surrounding protein environment because a previous study highlighted the importance of the protein environment in the spin-inversion mechanisms in $O_2$ binding to the heme protein.[10]

## 4. Concluding remarks

In this work we investigated the spin-inversion mechanisms in $O_2$ binding to a model heme complex using B97D DFT calculations. We used the mixed-spin Hamiltonian method to locate spin-inversion transition state structures between different total spin multiplicities. Nine spin-inversion structures were optimized for the singlet-triplet, singlet-quintet, triplet-quintet and quintet-septet spin-inversion processes. The singlet-triplet spin inversion occurred in the potential energy region at short Fe-O distances, whereas the singlet-quintet and quintet-septet spin inversions occurred in the longer Fe-

O distance region. We also performed on-the-fly BOMD calculations to further understand spin-inversion mechanisms. The out-of-plane motion of Fe plays a role in the spin-inversion mechanisms; however, quantum dynamics calculations, which can take into account the spin-vibronic effects, should be performed to fully understand the spin-inversion mechanisms in $O_2$ binding to the heme complex.

**Acknowledgements**

This work was supported by a Grant-in-Aid for Scientific Research from the Ministry of Education, Culture, Sports, Science and Technology of Japan (Grant No. 17KT0093).

## References


[1] K. P. Kepp, Heme: from quantum spin crossover to oxygen manager of life, *Coord. Chem. Rev*. **2017**, *344*, 363–374.

[2] S. Shaik, H. Chen, Lessens on $O_2$ and NO bonding to heme from ab initio multireference/multiconfiguration and DFT calculations, *J. Bio. Inorg. Chem*. **2011**, *16*, 841–855.

[3] B. F. Minaev, V. O. Minaeva, H. Ågren. Spin-Orbit Coupling in Enzymatic Reactions and the Role of Spin in Biochemistry. In: Handbook of Computational Chemistry. (Editor: J. Leszczynski), 2012, Springer, Dordrecht, 1067-1093.

[4] S. Franzen, Spin-dependent mechanism for diatomic ligand binding to heme, *Proc. Nat. Acad. Sci*. **2002**, *99*, 16754–16759.

[5] K. P. Jensen, U. Ryde, How $O_2$ binds to heme: reasons for rapid binding and spin inversion, *J. Bio. Chem*. **2004**, *279*, 14561–14569.

[6] H. Nakashima, J. Hasegawa, H. Nakatsuji, On the reversible $O_2$ binding of the Fe-porphyrin complex, *J. Comp. Chem*. **2006**, *27*, 426–433.

[7] J. Ribas-Ariño, J. J. Novoa, The mechanism for the reversible oxygen addition to heme. A theoretical CASPT2 study, *Chem. Comm*. **2007**, 3160–3162.

[8] N. Strickland, J. N. Harvey, Spin-forbidden ligand binding to the ferrous-heme group: Ab initio and DFT studies, *J. Phys. Chem*. **2007**, *111*, 841–852.

[9] M. Radoń, K. Pierloot, Binding of CO, NO, and $O_2$ to heme by density functional and multireference ab initio calculations, *J. Phys. Chem*. **2008**, *112*, 11824–11832.

[10] H. Chen, M. Ikeda-Saito, S. Shaik, Nature of the Fe–$O_2$ bonding in oxy-myoglobin: effect of the protein, *J. Am. Chem. Soc*. **2008**, *130*, 14778–14790.

[11] P. E. M. Siegbahn, M. R. A Blomberg, S.-L. Chen, Significant van der Waals effects in transition metal complexes, *J. Chem. Theo. Comp*. **2010**, *6*, 2040–2044.

[12] M. E. Ali, B. Sanyal, P. M. Oppeneer, Electronic structure, spin-states, and spin-crossover reaction of heme-related Fe-porphyrin: A theoretical perspective, *J. Phys. Chem*. **2012**, *116*, 5849–5859.

[13] K. P. Kepp, $O_2$ binding to heme is strongly facilitated by near-degeneracy of

electronic states, *ChemPhysChem* **2013**, *14*, 3551–3558.

[14] V. E. J. Berryman, R. J. Boyd, E. R. Johnson, Balancing exchange mixing in density-functional approximations for iron porphyrin, *J. Chem. Theo. Comp*. **2015**, *11*, 3022–3028.

[15] Y. Kitagawa, Y. Chen, N. Nakatani, A. Nakayama, J. Hasegawa, A DFT and multi-configurational perturbation theory study on $O_2$ binding to a model heme compound via the spin-change barrier, *Phys. Chem. Chem. Phys*. **2016**, *18*, 18137–18144.

[16] N. Kitagawa, M. Obata, T. Oda, Density functional study on positively charged six-coordinate $FeO_2$ porphyrin complex for a trigger of $O_2$ dissociation, *Chem. Phys. Lett*. **2016**, *643*, 119–125.

[17] T. Yang, M. G. Quesne, H. M. Neu, F. G. C. Reinhard, D. P. Goldberg, S. P. de Visser, Singlet versus triplet reactivity in an Mn(V)-Oxo species: Testing theoretical predictions against experimental evidence, *J. Am. Chem. Soc*. **2016**, *138*, 12375–12386.

[18] O. S. Siig, K. P. Kepp, Iron (II) and iron(III) spin crossover: Toward an optimal density functional, *J. Phys. Chem. A*, **2018**, *122*, 4208–4217.

[19] A. Lábas, D. K. Menyhárd, J. N. Harvey, J. Oláh, First principles calculation of the reaction rates for ligand binding to myoglobin: The cases of NO and CO, *Chem. Eur. J*. **2018**, 24, 5350–5358.

[20] D. Kurokawa, J. S. Gueriba, W. A. Diño, Spin-dependent $O_2$ binding to hemoglobin, *ACS Omega*, **2018**, *3*, 9241–9245.

[21] Q. M. Phung, K. Pierloot, The dioxygen adducts of iron and manganese porphyrins: electronic structure and binding energy, *Phys. Chem. Chem. Phys*. **2018**, *20*, 17009–17019.

[22] L. Du, F. Liu, Y. Li, Z. Yang, Q. Zhang, C. Zhu, J. Gao, Dioxygen Activation by Iron Complexes: The Catalytic Role of Intersystem Crossing Dynamics for a Heme-Related Model, *J. Phys. Chem. C* **2018**, *122*, 2821–2831.

[23] D. A. Scherlis, D. A. Estrin, Structure and spin-state energetics of an iron porphyrin model: An assessment of theoretical methods, *Int. J. Quantum Chem*. **2002**, *87*, 158–166.

[24] D. E. Bikiel, F. Forti, L. Boechi, M. Nardini, F. J. Luque, M. A. Martí, D. A. Estrin, Role of heme distortion on oxygen affinity in heme proteins: The protoglobin case, *J.*

*Phys. Chem. B* **2010**, *114*, 8536–8543.

[25] S. R. Badu, R. H. Pink, R. H. Scheicher, A. Dubey, N. Sahoo, K. Nagamine, T. P. Das, First principles electronic structure investigation of order of singlet and triplet states of oxyhemoglobin and analysis of possible influence of muon trapping, *Hyperfine Interact*. **2010**, *197*, 331–340.

[26] T. Saito, Y. Kataoka, Y. Nakanishi, T. Matsui, Y. Kitagawa, T. Kawakami, M. Okumura, K. Yamaguchi, Theoretical studies of the effect of orientation of ligands and spin contamination error on the chemical bonding in the $FeO_2$ core in oxymyoglobin, *J. Mol. Struct.: THEOCHEM* **2010**, *954*, 98–104.

[27] B. Yang, L. Gagliardi, D. G. Truhlar, Transition states of spin-forbidden reactions, *Phys. Chem. Chem. Phys*. **2018**, *20*, 4129–4136.

[28] T. Takayanagi, T. Nakatomi, Automated reaction path searches for spin-forbidden reactions, *J. Comp. Chem*. **2018**, *39*, 1319–1326.

[29] T. Nakatomi, S. Koido, Y. Watabe, T. Takayanagi, Spin-inversion mechanisms in the reactions of transition metal cations ($Sc^+$, $Ti^+$, $V^+$, $Cr^+$, $Mn^+$, $Fe^+$, $Co^+$, $Ni^+$, and $Cu^+$) with OCS in the gas phase: a perspective from automated reaction path search calculations, *Int. J. Quantum Chem*. **2019**, *119*, e25908.

[30] M. Kawano, S. Koido, T. Nakatomi, Y. Watabe, T. Takayanagi, Automated reaction path search calculations of spin-inversion mechanisms in the $^{6,4,2}Nb + C_2H_4$ reaction, *Comp. Theo. Chem*. **2019**, *1115*, 31–37.

[31] T. Takayanagi, K. Saito, H. Suzuki, Y. Watabe, T. Fujihara, Computational analysis of two-state reactivity in $\beta$-hydride elimination mechanisms of Fe(II) and Co(II)-alkyl complexes, *Organometallics* **2019**, *38*, 3582–3589.

[32] S. Grimme, Semiempirical GGA-type density functional constructed with a long-range dispersion correction, *J. Comp. Chem*. **2006**, *27*, 1787–1799.

[33] M. Swart, A new family of hybrid density functionals, *Chem Phys Lett*. **2013**, *580*, 166–171.

[34] M. J. Frisch, G. W. Trucks, H. B. Schlegel, G. E. Scuseria, M. A. Robb, J. R. Cheeseman, G. Scalmani, V. Barone, B. Mennucci, G. A. Petersson, H. Nakatsuji, M. Caricato, X. Li, H. P. Hratchian, A. F. Izmaylov, J. Bloino, G. Zheng, J. L. Sonnenberg,

M. Hada, M. Ehara, K. Toyota, R. Fukuda, J. Hasegawa, M. Ishida, T. Nakajima, Y. Honda, O. Kitao, H. Nakai, T. Vreven, J. A. Montgomery, jr., J. E. Peralta, F. Ogliaro, M. Bearpark, J. J. Heyd, E. Brothers, K. N. Kudin, V. N. Staroverov, R. Kobayashi, J. Normand, K. Raghavachari, A. Rendell, J. C. Burant, S. S. Iyengar, J. Tomasi, M. Cossi, N. Rega, J. M. Millam, M. Klene, J. E. Knox, J. B. Cross, V. Bakken, C. Adamo, J. Jaramillo, R. Gomperts, R. E. Stratmann, O. Yazyev, A. J. Austin, R. Cammi, C. Pomelli, J. W. Ochterski, R. L. Martin, K. Morokuma, V. G. Zakrzewski, G. A. Voth, P. Salvador, J. J. Dannenberg, S. Dapprich, A. D. Daniels, Ö. Farkas, J. B. Foresman, J. V. Ortiz, J. Cioslowski and D. J. Fox, *Gaussian 09*, Revision D.01, Gaussian, Inc., Wallingford, CT, USA, 2009.

[35] S. Maeda, Y. Osada, K. Morokuma, K. Ohno, GRRM 11: http://grrm.chem.tohoku.ac.jp/GRRM/ (accessed on Jan. 7, 2018).

[36] K. Ohno, S. Maeda, A Scaled Hypersphere Search Method for the Topography of Reaction Pathways on the Potential Energy Surface, *Chem. Phys. Lett*. **2004**, *384*, 277–282.

[37] S. Maeda, K. Ohno, Global Mapping of Equilibrium and Transition Structures on Potential Energy Surfaces by the Scaled Hypersphere Search Method: Applications to Ab Initio Surfaces of Formaldehyde and Propyne Molecules, *J. Phys. Chem. A* **2005**, *109*, 5742–5753.

[38] K. Ohno, S. Maeda, Global Reaction Route Mapping on Potential Energy Surfaces of Formaldehyde, Formic Acid, and their Metal Substituted Analogues, *J. Phys. Chem. A* **2006**, *110*, 8933–8941.

[39] S. Maeda, K. Ohno, K. Morokuma, Updated Branching Plane for Finding Conical Intersections without Coupling Derivative Vectors, *J. Chem. Theo. Comp*. **2010**, *6*, 1538–1545.

[40] S. Giuseppe, M. Leopoldini, MolSOC: A Spin-Orbit Coupling Code. *Comp. Phys. Comm*. **2014**, *185*, 676–683.

[41] J. M. Millam, V. Bakken, W. Chen, W. L. Hase, B. H. Schlegel, Ab initio classical trajectories on the Born–Oppenheimer surface: Hessian-based integrators using fifth-order polynomial and rational function fits, *J. Chem. Phys*. **1999**, *111*, 3800–3805.

[42] S. Iuchi, N. Koga, An improved model electronic Hamiltonian for potential energy surfaces and spin−orbit couplings of low-lying d−d states of $[Fe(bpy)_3]^{2+}$, *J. Chem. Phys*. **2014**, *140*, 024309.

[43] C. Sousa, A. Domingo, C. de Graaf, Effect of second-order spin-orbit coupling on the interaction between spin states in spin-crossover systems, *Chem. Eur. J*. **2018**, *24*, 5146–5152.

[44] Y. Shiota, D. Sato, G. Juhász, K. Yoshizawa, Theoretical study of thermal spin transition between the singlet state and the quintet state in the $[Fe(2\text{-picolylamine})_3]^{2+}$ spin crossover system, *J. Phys. Chem. A* **2010**, *114*, 5862–5869.

[45] K. Falahati, H. Tamura, I. Burghardt, M. Huix-Rotllant, Ultrafast carbon monoxide photolysis and heme spin-crossover in myoglobin via nonadiabatic quantum dynamics, *Nat. Comm*. **2018**, *9*, 4502.

[46] T. J. Penfold, E. Gindensperger, C. Daniel, C. M. Marian, Spin-vibronic mechanism for intersystem crossing, *Chem. Rev*. **2018**, *118*, 6975–7025.

[47] J. N. Harvey, M. Aschi, H. Schwarz, W. Koch, The singlet and triplet states of phenyl cation. A hybrid approach for locating minimum energy crossing points between non-interacting potential energy surfaces, *Theo. Chem. Acc*. **1998**, *99*, 95–99.

[48] M. Torrent-Sucarrat, I. Arrastia, A. Arrieta, F. P. Cossío, Stereoselectivity, Different Oxidation States, and Multiple Spin States in the Cyclopropanation of Olefins Catalyzed by Fe–Porphyrin Complexes, *ACS Catal*. **2018**, *8*, 11140–11153.

[49] D. A. Fedorov, S. R. Pruitt, K. Keipert, M. S. Gordon, S. A. Varganov, Ab initio multiple spawning method for intersystem crossing dynamics: Spin-forbidden transitions between $^3B_1$ and $^1A_1$ states of $GeH_2$, *J. Phys. Chem. A* **2016**, *120*, 2911–2919.

[50] D. A. Fedorov, A. O. Lykhin, S. A. Varganov, Predicting intersystem crossing rates with AIMS-DFT molecular dynamics, *J. Phys. Chem. A* **2018**, *122*, 3480–3488.

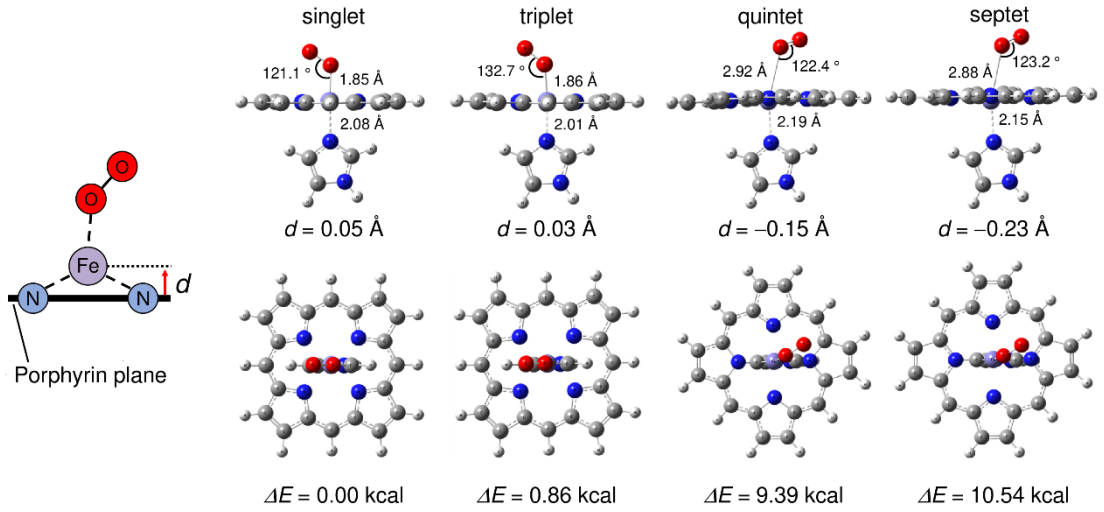


**Figure 1:** Optimized structures of the $O_2$-FePorIm complex in the singlet to septet spin states calculated at the B97D level of theory. One of the four structures for each spin state is shown. See the main text for detail. The Fe out-of-plane distance ($d$) and relative energies ($\Delta E$) measured from the most stable singlet minimum are also presented.

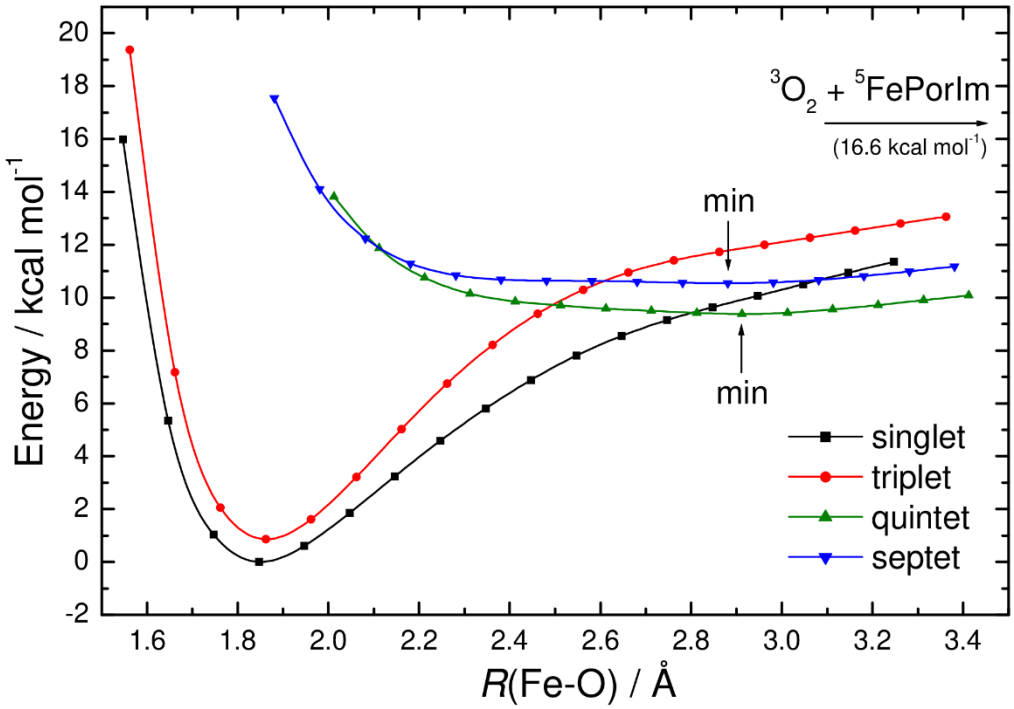


**Figure 2:** Calculated one-dimensional potential energy curves for singlet, triplet, quintet, and septet states as a function of the Fe–O distance. Other geometric parameters are fully optimized with respect to energy. The energy is measured from the most stable singlet minimum structure. The asymptotic energy level of the $^3O_2$ + $^5$FePorIm dissociation limit is also shown.

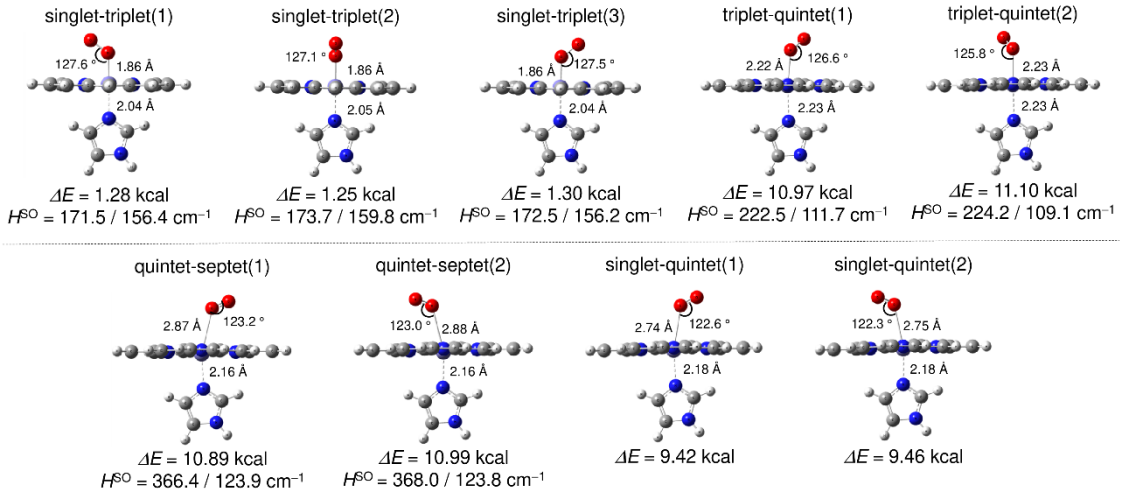


**Figure 3:** Spin-inversion structures optimized on the mixed-spin potential energy surfaces. Geometric parameters and relative energies ($\Delta E$ in kcal/mol) measured from the most stable singlet minimum structure are also presented. Spin-orbit coupling constants (maximum and averaged values in $cm^{-1}$, see text for detail) calculated at the spin-inversion structure are also shown.

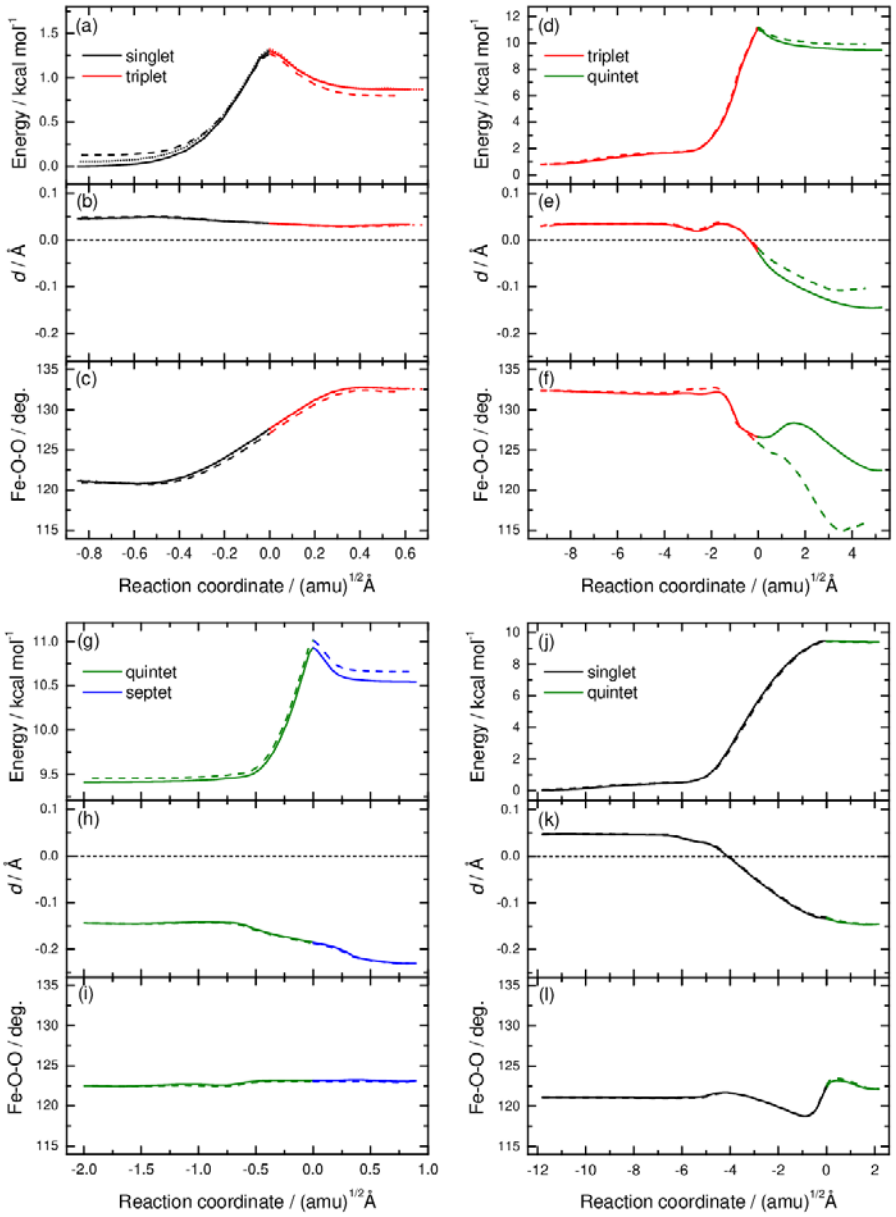


**Figure 4:** IRC potential energy profiles for singlet-triplet (left upper panel), triplet-quintet (right upper panel), quintet-septet (left lower panel), and singlet-quintet (right lower panel) spin-inversion processes. The results were obtained at the B97D level of theory. Notice that IRC profiles from each spin-inversion transition state are represented by different line styles. For each panel, changes in geometric parameters (Fe–O–O angle and deviation distance, *d*) along the IRC are shown.

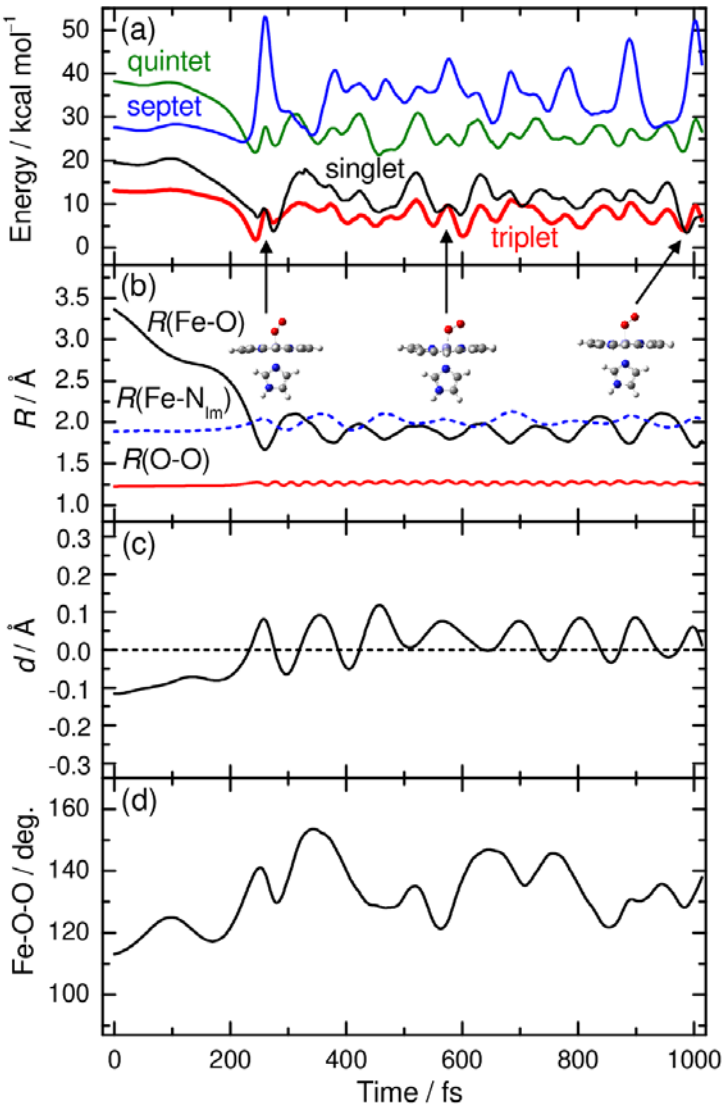


**Figure 5:** BOMD trajectory calculated on the triplet potential energy surface. (a) Energies for the four spin states plotted as a function of time, where the triplet state is indicated by the bold line. (b) Fe–O, O–O, and Fe-N(Im) distances, (c) Fe deviation distance, *d*, and (c) Fe–O–O angle as a function of time.

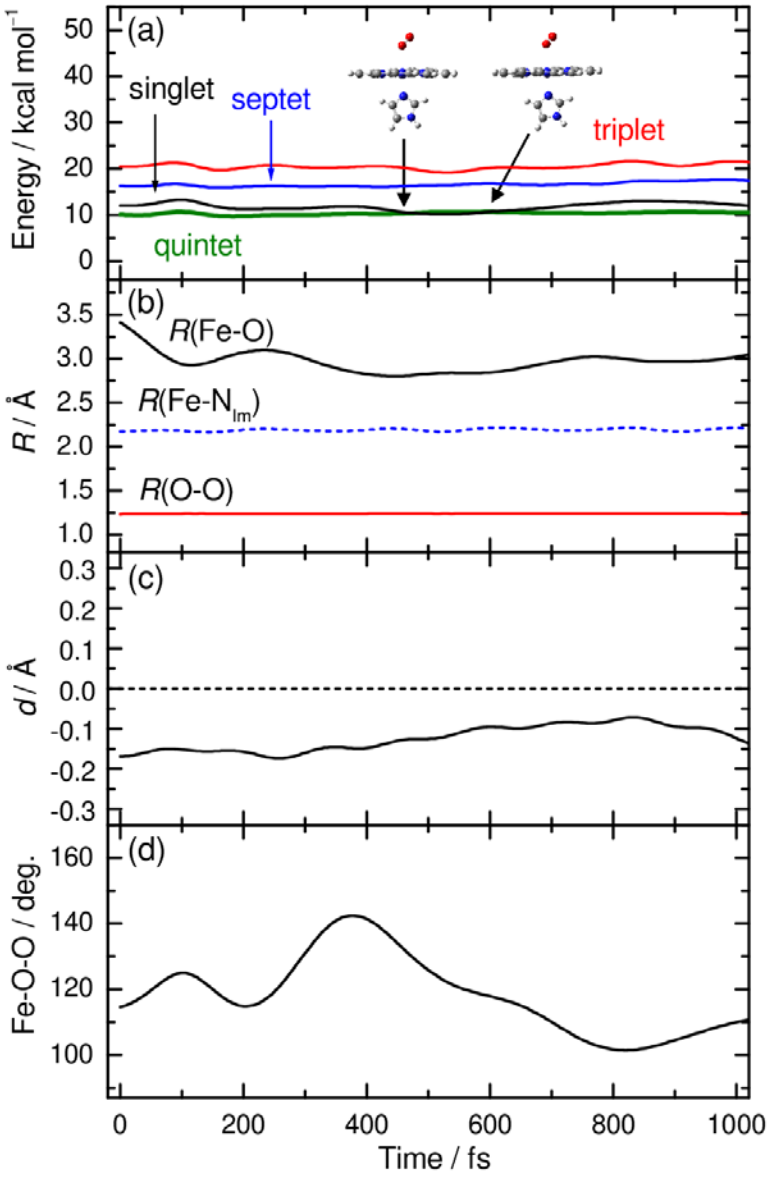


**Figure 6:** BOMD trajectory calculated on the quintet potential energy surface. (a) Energies for the four spin states as a function of time, where the quintet state is indicated by the bold line. (b) Fe–O, O–O, and Fe-N(Im) distances, (b) Fe deviation distance, *d*, and (c) Fe–O–O angle as a function of time.

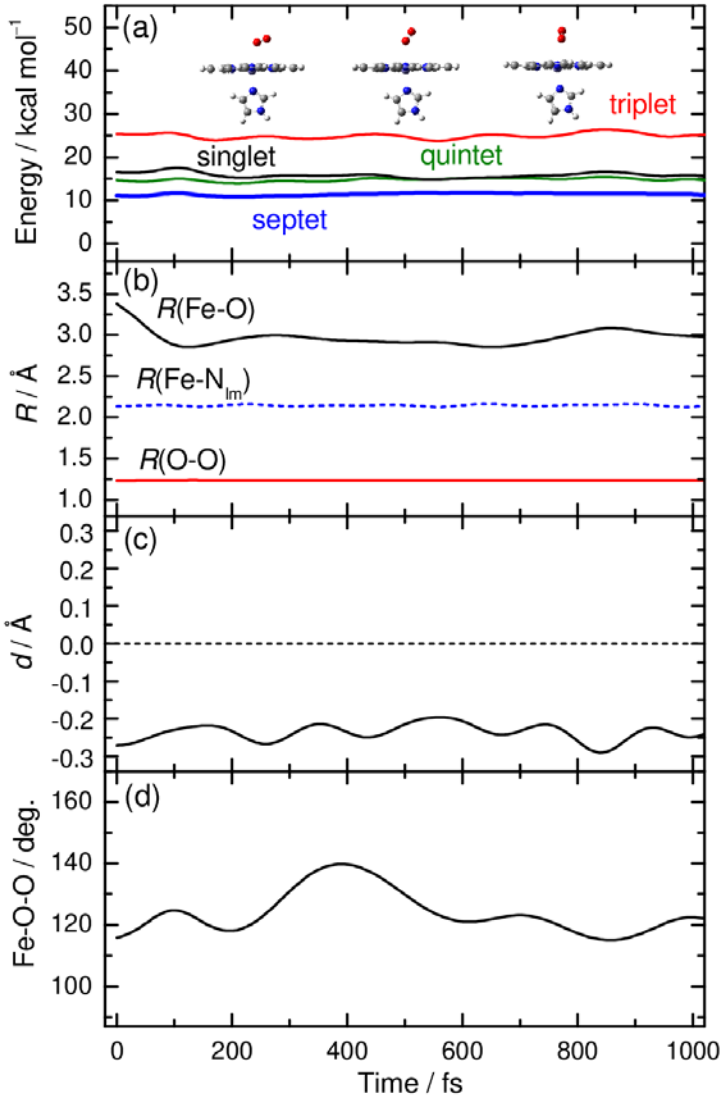


**Figure 7:** BOMD trajectory calculated on the septet potential energy surface. (a) Energies for the four spin states as a function of time, where the septet state is indicated by the bold line. (b) Fe–O, O–O, and Fe-N(Im) distances, (c) Fe deviation distance, *d*, and (d) Fe–O–O angle as a function of time.

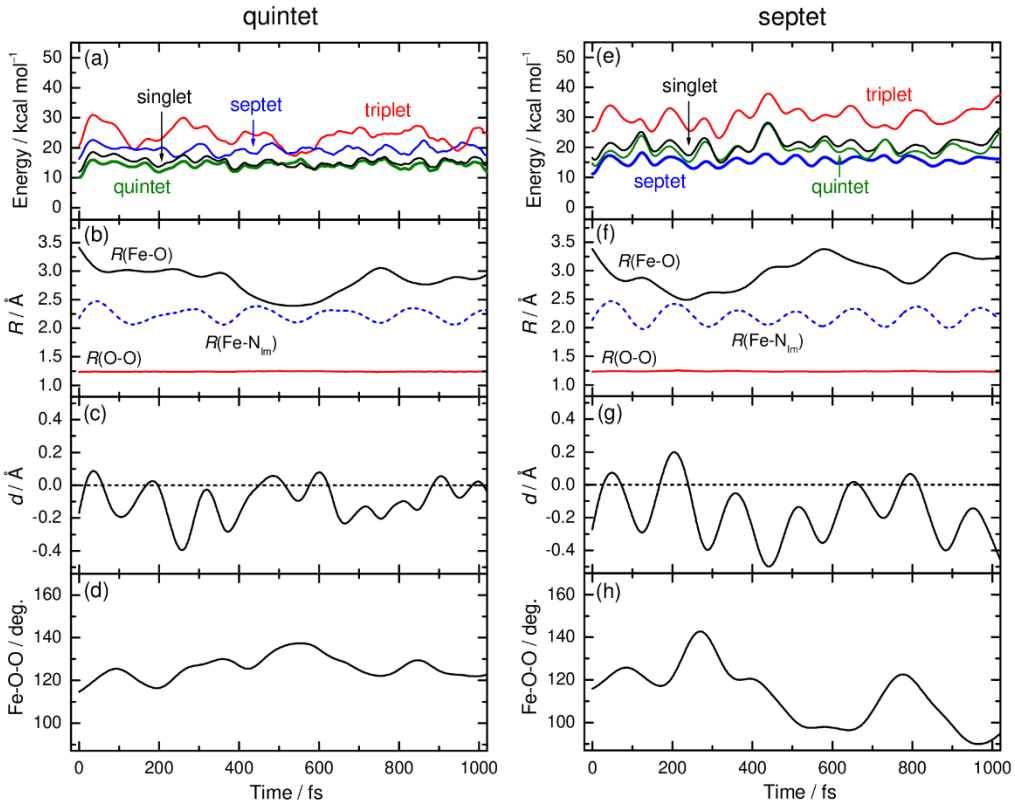


**Figure 8:** BOMD trajectory calculated on the quintet (left panels) and septet (right panels) potential energy surfaces, where the initial kinetic energy of Fe along the *d* coordinate is set to 10 kcal/mol. (a) and (e) Potential energies for the four spin states as a function of time. (b) and (f) Fe–O, O–O, and Fe-N(Im) distances, (c) and (g) Fe out-of-plane distance, *d*, and (d) and (h) Fe–O–O angle as a function of time.

**Table of Contents**

Spin-inversion mechanisms of the $O_2$ binding by heme were studied using density-functional theory calculations. We applied the mixed-spin Hamiltonian method to locate spin-inversion structures between different total spin multiplicities. A total of nine spin-inversion structures were successfully identified. We also performed on-the-fly Born-Oppenheimer molecular dynamics calculations to understand the effect of nuclear dynamics in the spin-inversion processes.